remote sensing

MDPI

Article

Advancing Sea Surface Height Retrieval through Global Navigation Satellite System Reflectometry: A Model Interaction Approach with Cyclone Global Navigation Satellite System and FengYun-3E Measurements

Jin Xing [1], Dongkai Yang [1,2], Zhibo Zhang [1] and Feng Wang [1,*]

[1] School of Electronic and Information Engineering, Beihang University, Beijing 100191, China; jinxing@buaa.edu.cn (J.X.); edkyang@buaa.edu.cn (D.Y.); zhangzhibo94@buaa.edu.cn (Z.Z.)
[2] International Innovation Institute, Beihang University, Hangzhou 311115, China
* Correspondence: b20113@buaa.edu.cn

Abstract: The measurement of sea surface height (SSH), which is of great importance in the field of oceanography, can be obtained through the innovative technique of GNSS-R for remote sensing. This research utilizes the dataset from spaceborne GNSS-R platforms, the Cyclone Global Navigation Satellite System (CYGNSS) and FengYun-3E (FY-3E), as the primary source of data for retrieving sea surface height (SSH). The utilization of artificial neural networks (ANNs) allows for the accurate estimation of ocean surface height with a precision of meter-level accuracy throughout the period of 1–17 August 2022. As a traditional machine learning method, an ANN is employed to extract pertinent data features, facilitating the acquisition of precise sea surface height estimations. Additionally, separate models are devised for both GNSS-R platforms, one based on constant velocity (CV) and the other on constant acceleration (CA). The Interactive Multiple Model (IMM) is utilized as the main method to combine the four models and convert the likelihood of each model. The transition between the models allows the filters to effectively adapt to dynamic changes and complex environments. This approach relies on the fundamental notion of the Kalman filter (KF), which showcases robust noise handling capabilities in predicting the SSH, separately. The results demonstrate that the model interaction technology is capable of efficiently filtering and integrating SSH data, yielding a Root Mean Square Error (RMSE) of 1.03 m. This corresponds to a 9.84% enhancement compared to the retrieved height from CYGNSS and a 37.19% enhancement compared to the retrieved height from FY-3E. The model proposed in this paper provides a potential scheme for the GNSS-R data fusion of multiple platforms and multiple models. In the future, more data sources and more models can be added to achieve more accurate adaptive fusion.

Keywords: spaceborne GNSS-R; CYGNSS and FY-3E; interactive multiple model; Kalman filter

check for updates

Citation: Xing, J.; Yang, D.; Zhang, Z.; Wang, F. Advancing Sea Surface Height Retrieval through Global Navigation Satellite System Reflectometry: A Model Interaction Approach with Cyclone Global Navigation Satellite System and FengYun-3E Measurements. *Remote Sens.* **2024**, *16*, 1896. https://doi.org/10.3390/rs16111896

Academic Editors: Xuerui Wu, Kousuke Heki, Andrés Calabia and Xinggang Zhang

Received: 19 April 2024
Revised: 15 May 2024
Accepted: 21 May 2024
Published: 24 May 2024

1. Introduction

The growing subject of ocean technology has garnered unprecedented worldwide attention. In the field of oceanographic research, it has become extremely important to ensure quality and simultaneously monitor the environment [1,2]. Utilizing sea surface height data in ocean research enables a convincing examination of the effects of global climate change on the melting of polar ice, the expansion of saltwater due to temperature changes, and alterations in atmospheric and marine circulation systems [3]. The measurement of sea surface height variations is crucial for oceanographic research, since they provide essential indications of dynamic changes in the marine environment [4]. To comprehensively investigate significant characteristics of ocean fluid dynamics, such as tidal forces, ocean currents, and the prediction of ocean disasters, it is necessary to continuously monitor sea level. At present, methods for determining sea surface height include the use of tidal gauges and ocean altimetry satellites [5,6]. However, these methods have their limitations. Tidal gauges can be affected by vertical crustal movements, while spaceborne altimeters have long revisit periods and are cost-intensive [7,8]. GNSS-R technology shows great potential in the field of remote sensing due to its advantages. With the development of various spaceborne systems, a wider variety of navigation satellites have contributed to the data sources utilized in GNSS-R technology [9]. In 2014, the Surrey Satellite Company in the United Kingdom initiated the launch of the TDS-1 satellite [10]. Subsequently, in 2016, NASA successfully launched CYGNSS [11], and in 2019, China launched the Bufeng-1 A/B satellite [12]. These missions have significantly broadened the horizons for GNSS-R applications in space [13]. The availability of signal sources makes GNSS-R technology suitable for a wide range of applications, such as soil moisture [14–16], ice [17–20], flood [21,22], and sea wind [23], in recent years. In sea level altimetry, GNSS-R also proves valuable for its precision and spatial resolution advantages [24–26].

The GNSS-R technique for sea level altimetry was first introduced by Martin in 1993 [27]. The viability of retrieving sea surface height using spaceborne GNSS-R is assessed through simulations and experiments, which are conducted as a passive remote sensing method [28]. The research reveals that employing the carrier phase can achieve accuracy at the centimeter level. The reflected signals obtained from the TDS-1 (TechDemosat-1) satellite are used to extract SSH measurements. In [29], the reflected signals from TDS-1 satellites are utilized to extract measurements of sea surface height, which are then compared to the DTU10 data. When the surface is covered by ice, the reflected signal exhibits an increased coherence, resulting in a more precise RMSE of 4.7 cm [30]. Further analysis of the TDS-1 data in SSH retrieval revealed the result, as demonstrated by the achievement of a precision of 4.1 m during a 6 s integration period utilizing the code phase approach [31]. Carrier phase altimetry provides higher accuracy but requires more specific environmental conditions. Cardellach demonstrates a precision of 4.1 cm, indicating that coherent scattering is achievable when the wind speed is below 6 m/s and the wave height is less than 1.5 m [32]. Researchers have extensively studied continuity and optimization in the detection and processing of coherent signals. This includes the development of coherence assessment algorithms and the use of Kalman filtering for accurate carrier phase predictions [33,34].

Therefore, although code phase height measurement may not attain very precise accuracy, it is applicable in a broader variety of conditions. Furthermore, researchers have been actively engaged in studies aimed at enhancing accuracy through the use of the code phase altimetry method. In 2020, Mashburn introduced a delayed retracking approach that relies on the reflection model [35]. The authors verified the effectiveness of their approach by utilizing CYGNSS data collected in Indonesia, leading to a more accurate measurement. The leading edge derivatives (LEDs) of spaceborne GNSS-R waveforms are employed and enhanced to retrieve sea surface height in [36]. A correction method is introduced for satellite altitude angles in the detection of sea surface height in [37]. The authors employ model-driven and data-driven methodologies in this study to improve the effects of elevation angle. Machine learning has recently emerged as a promising tool in the field of GNSS-R altimetry and can be employed for data feature extraction and sea surface height retrieval. The utilization of PCA-SVR and Convolutional Neural Networks (CNNs) demonstrates the effectiveness of machine learning in GNSS-R remote sensing applications [38]. CNNs have the advantage of being able to automatically extract the GNSS-R's features [39]. The F-ResNet was developed by utilizing CYGNSS data and employing the FrFT method to filter the Delay Doppler Map (DDM) [40]. Subsequently, an improved ResNet network was established for the purpose of retrieving SSH. Another method employed in machine learning involves utilizing parametric mode decomposition with spaceborne data from the QZSS-R platform [41], using L1, L2, and L5 signals to retrieve the respective correlation coefficients. Furthermore, different spaceborne platforms operate in different orbits, resulting in different geometry configurations of reflected signals on the Earth's surface over time. A variety of environmental factors and specific characteristics of the spaceborne platform have a substantial impact on the retrieved results. Reference [42] analyzes and discusses the data obtained by different spaceborne platforms for remote sensing. Therefore, the purpose of this work is to improve the precision of retrieved results by integrating data from several platforms.

The IMM algorithm, based on Bayesian theory, enables the transition between models [43]. Each model operates concurrently, passes through a Markov probability matrix and the updated probability of each model to switch models, and then chooses the model that best fits the actual circumstance [44]. It is commonly used in modern, intricate estimation problems. Due to the inherent inaccuracy of single-model formation, its usage is primarily limited to moving target identification and speech recognition [45]. In this paper, it is used in GNSS-R altimetry on multiple platforms with different models.

When conducting spaceborne GNSS-R SSH retrieval, it is common practice to designate a specific time window for calculating average results within a gridded area. Expanding the coverage helps to avoid anomalies in the data that may occur within a single system.

As shown in Figure 1, we first download the CYGNSS and FY-3E data. Then, we use the feature values and feed them into the network. The result is the height of the sea surface. Then, we store the trained network parameters. Next, we mesh the ocean surface. For the same cell, there will be retrieved data from CYGNSS or FY-3E systems, or both, or neither. We design four models, which are based on the Kalman filter. Two of them are developed using CYGNSS's retrieved results. The other two are from FY-3E's retrieved results. The IMM-KF approach presented in this paper facilitates adaptive model selection at different time intervals, resulting in a dynamic allocation of weight and probability, ultimately culminating in the fusion of SSH data.

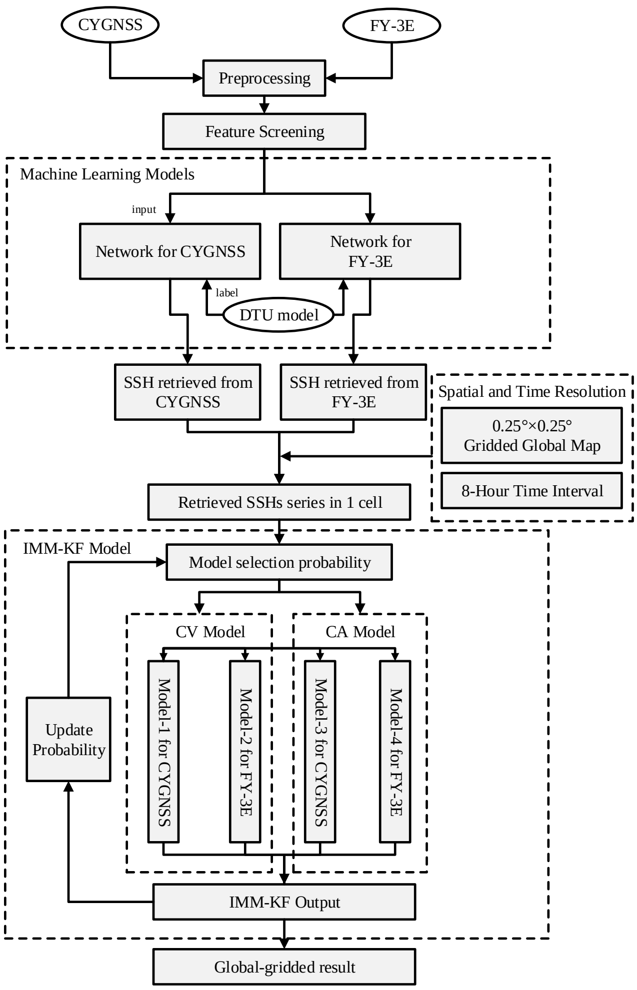

Figure 1. Data processing flow chart.

The contributions of this research are as follows:

- This research demonstrates the effective use of ANNs for retrieving SSHs from datasets provided by the spaceborne GNSS-R platforms CYGNSS and FY-3E, achieving meter-level precision in SSH estimations.
- The research develops distinct models, each utilizing KF, with implementations based on either CV or CA to describe changes in SSH.
- This research employs the IMM-KF as the method for integrating and managing the likelihood conversion of four distinct models. It enables the adaptation of the filters to dynamic changes and complex environments.

The following sections are structured as follows: Section 2 provides a framework for the methodology and developing models. Section 3 presents the obtained results and provides the discussion and analysis. Section 4 is the conclusion.

2. Methodology

2.1. GNSS-R Altimetry Principle Using DDM

In spaceborne altimetry, the usual method is utilizing geometric principles to determine the delay in signal propagation. Subsequently, this signal arrives at the surface of the ocean and is scattered. The antenna receives the reflected signals and the signals are processed to different outputs, such as DDM. In the processing of the reflected signal, the GNSS-R receiver generates a local replication with different time delays and Doppler frequencies and then correlates the local replication with the received reflected signal. The antenna receives the reflected signals with different delays and Dopplers. Thus, the DDM can be acquired to show the characteristics of the surface. The Z-V model, which is the bistatic radar equation used for GNSS reflected signals, is responsible for generating the DDMs [46]. In a DDM, when applied to a smooth surface, the delay of the maximum power corresponds to the specular point. Then, the DDM bins are computed by:

$$\left\langle |Y(\tau,f)|^2 \right\rangle = \frac{\lambda^2 T_i^2}{(4\pi)^3} P_t G_t \iint \frac{G_r \Lambda^2(\tau) S^2(f)}{R_t^2 R_r^2} \sigma_0 \mathrm{d}s, \tag{1}$$

where τ represents the delay, f represents the Doppler frequency, T_i represents the coherent integration time, and λ represents the carrier wavelength. P_t is the transmission power of the GNSS satellite, and G_t and G_r represent the gain of the transmitting and receiving antennas, respectively. $\Lambda^2(\tau)$ and $S^2(f)$ are the Woodward Ambiguity Function (WAF) and the Doppler shift function. R_t and R_r represent the distance from the transmitter to the receiver and the receiver to the element ds on the surface, respectively. σ_0 represents the normalized bistatic radar scattering section (NBRCS).

The range for SSH retrieval is achieved by measuring the pseudo-code phase and carrier phase.

Figure 2 shows the geometric principle. The current point of specular reflection occurs on the surface of the sea, while the point of specular reflection for the model is on the WGS84 ellipsoidal surface. The delay in the propagation path is determined by the geometric relationship illustrated in the image. α represents the incidence angle. R_d is the distance from the transmitter to the receiver. R_r and R_t are the distance from the specular point on the sea surface to the receiver and transmitter, respectively.

The distances from the specular point on the ellipsoid to the receiver and the transmitter are R'_r and R'_t, respectively. According to the geometric relationship, H_t and H_r are the height of the transmitter and the receiver. Therefore, SSH is described as:

$$\mathrm{SSH} = \frac{(R'_t + R'_r - R_d) - (R_t + R_r - R_d)}{2\cos\alpha}. \tag{2}$$

where α is the reflection incidence angle at the surface. This trigonometric relationship is derived by assuming that [35] (1) the transmitter is far away enough that the incident ray paths at the surface can be considered parallel and (2) the reflecting surface is flat. As shown in Figure 3, we use CYGNSS orbital parameters for simulation to obtain the height retrieval error, which is limited to 2.5 mm.

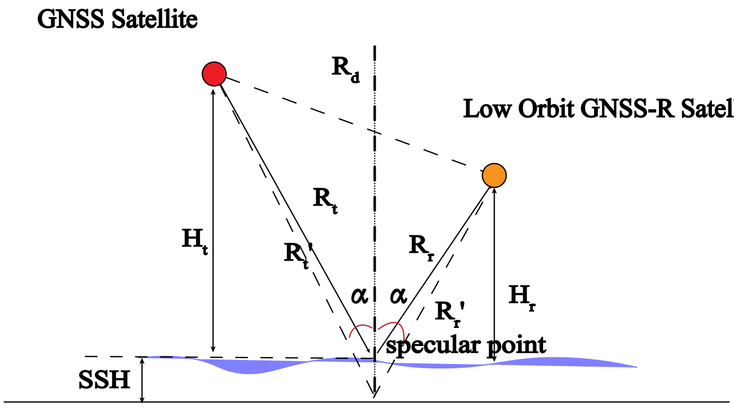

Figure 2. Geometric relationship diagram of space GNSS-R.

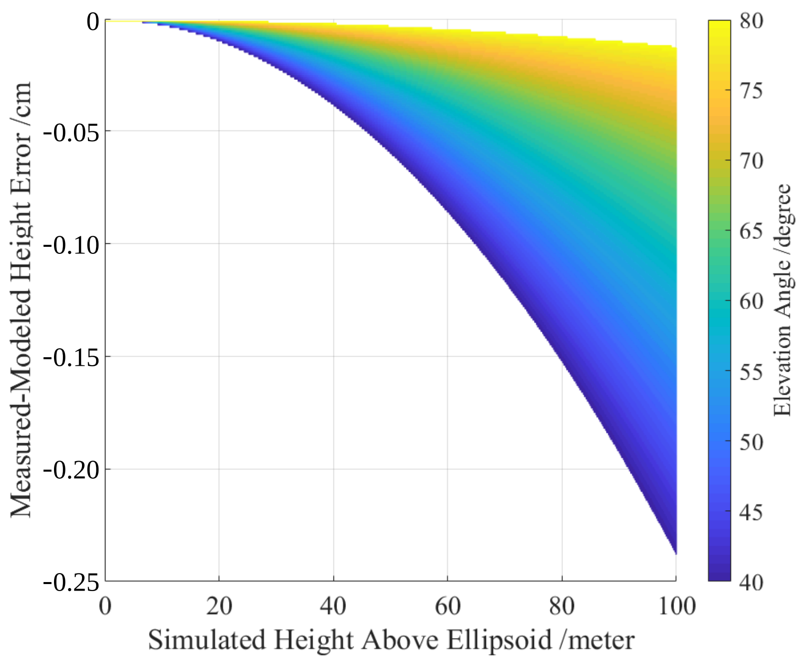

Figure 3. Estimated error from linearized delay to height mapping.

2.2. Machine Learning SSH Retrieved Model

2.2.1. Dataset Preparation

The present study employs data from two GNSS-R platforms: CYGNSS and FY-3E.

CYGNSS is a microsatellite satellite system developed by NASA with the primary objective of monitoring and researching on cyclones [11]. This platform includes eight microsatellites. The content of CYGNSS's Level 1 data comprises the observation data, such as DDMs and other information. This paper uses the Level 1 V3.1 data of CYGNSS from 1–17 August 2022. Another data source we use is FY-3E, which China developed. FY-3E is equipped with the Global Navigation Satellite System Occultation Sensor II (GNSSO-II) instrument, which is purposed to procure the occultation observation data of signals emanating from the GNSS satellite [47]. Both GNSS-R platforms employ a left-hand circular polarization antenna to gather reflected signals from GNSS satellites. The reflected signals are processed by the correlation procedures with locally generated pseudorandom codes, resulting in the production of DDMs. The raw counts of the example DDMs are displayed in Figure 4 for the CYGNSS and FY-3E platforms.

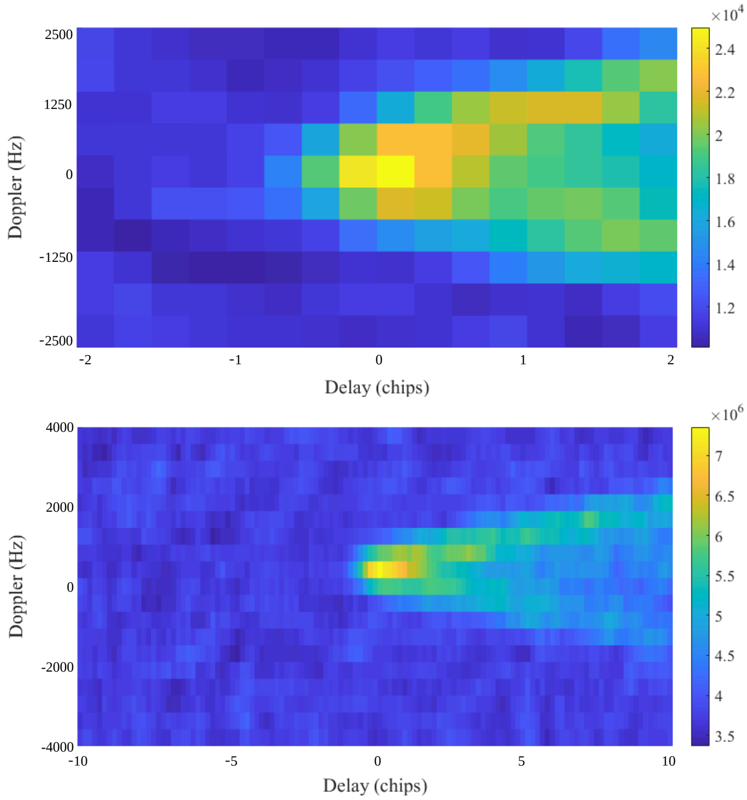

Figure 4. Example DDMs of CYGNSS and FY-3E with 17 × 11 and 122 × 20 pixels, respectively.

Currently, most GNSS-R ocean altimetry studies depend on the DTU global ocean tide model to establish SSHs as the ground-truth data [48]. The DTU global SSH model is constructed from a synthesis of data collected from diverse altimetry satellites [49]. This model precisely computes tidal heights based on input parameters including Julian Day time and longitude/latitude. The SSH results SSH_{ground_truth} can be obtained by:

$$SSH_{ground\_truth} = h_{MSS} + h_{Tide}, \tag{3}$$

where h_{MSS} is the MSS result from the DTU21 global SSH model and h_{Tide} is the result from the DTU global ocean tide model.

2.2.2. Training and Validation

The primary focus of this research is not on the novelty of machine learning network architecture. Therefore, a classical ANN is employed to achieve SSH. The network will not be excessively elaborate.

We select the data from 1 and 2 August 2022 for the network training. The training and validation set ratio is determined to be 7:3. The DTU dataset is utilized as the specified target variable for both training the network and evaluating the precision of the predicted results.

In the process of feature extraction, the incorporation of physical models assumes a crucial role in identifying the pertinent features for machine learning. Within the scope of this investigation, we have opted for parameters associated with the DDM peak specifically for CYGNSS and FY-3E. The selection of these parameters is predicated on the signal-to-noise ratio (SNR) of the receiving antenna and its antenna gain. When calculating SSH using traditional geometric methods, it becomes imperative to take into account the geometric coordinates of both the receiving and transmitting antennas, as well as the coordinates of the specular points. Furthermore, considering the velocities of both the transmitter and receiver plays a crucial role in attaining more accurate retrieval outcomes. Furthermore, the parameters specific to each platform are detailed in Table 1 below, along with their respective descriptions.

Table 1. The input parameters of the network from CYGNSS and FY-3E.

CYGNSS	FY-3E	Description
tx_pos_x, tx_pos_y, tx_pos_z	Tx_pos_x, Tx_pos_y, Tx_pos_z	The position of the transmitter in the X, Y, Z directions
tx_vel_x, tx_vel_y, tx_vel_z	Tx_vel_x, Tx_vel_y, Tx_vel_z	The velocity of the transmitter in the X, Y, Z directions
rx_pos_x, rx_pos_y, rx_pos_z	Rx_pos_x, Rx_pos_y, Rx_pos_z	The position of the receiver in the X, Y, Z directions
rx_vel_x, rx_vel_y, rx_vel_z	Rx_vel_x, Rx_vel_y, Rx_vel_z	The velocity of the receiver in the X, Y, Z directions
sp_inc_angle	Sp_inc_angle	The incidence angle of the specular point
$gps\_ant\_gain\_db\_i$	$Sp\_antenna\_gain$	The antenna gain of the receiver antenna in the direction of the specular point
ddm_snr	\	The DDM peak signal-to-noise ratio
\	Ddm_sp_snr	The DDM specular point signal-to-noise ratio
\	Ddm_sp_delay	The DDM specular point delay
\	Ddm_peak_delay	The DDM peak delay
\	$Ddm\_sp\_doppler$	The DDM specular point Doppler shift
$add\_range\_to\_sp$	\	The additional range to the specular point

CYGNSS comprises 16 inputs, while FY-3E comprises 19 inputs, with DTU data serving as the designated labels. The ANN network for CYGNSS data has four layers with {20, 20, 20, 10} nodes in the corresponding layers. The network for FY-3E data has five layers with {32, 16, 8, 4, 2} nodes in the corresponding layers. The input data are normalized feature-wise to zero mean and unit variance, and we employ 1000 epochs.

2.3. SSH Processing Model Based on Kalman Filter

This study utilizes the SSH obtained through independent retrieval of data from the CYGNSS and FY platforms. In the previous subsection, machine learning techniques are used to calculate the SSH of individual specular points. Based on the results obtained from each system during a specific period, different models are developed to describe the SSH results. These models are referred to as constant velocity (CV) and constant acceleration (CA) models, indicating that the SSH can be represented by either a CV or CA model.

The variability of the SSH has the potential to achieve filtration and prediction. After averaging, it can be postulated that the alterations in the SSH caused by wind and waves have been effectively eradicated. Consequently, the MSS is utilized as the basis for our model. The global MSS can be analyzed by dividing global regions into distinct grids, each representing a unique spatial domain. Our proposed model can filter and predict the subsequent state by relying on the preceding state.

Following acquiring the MSS data, the Kalman filter is subsequently employed. Traditional methods can predict the MSS in the temporal dimension for one GNSS-R platform. We define the state vector at the k-th time interval as:

$$\mathbf{h}[k] = \begin{bmatrix} h[k] & \dot{h}[k] & \ddot{h}[k] \end{bmatrix}^{\mathrm{T}}, \tag{4}$$

where $h[k]$ represents the SSH and $\dot{h}[k]$ and $\ddot{h}[k]$ represent the first-order derivative and second-order derivative of the MSS, respectively.

The measurements are modeled as

$$y[k] = \mathbf{H}\mathbf{h}[k] + v[k], \tag{5}$$

where $\mathbf{H} = \begin{bmatrix} 1 & 0 & 0 \end{bmatrix}$ and $v[k]$ is the measurement noise.

With the supposed model of the MSS, the state $\mathbf{h}$ is predicted as:

$$\mathbf{h}^{-}[k+1] = \mathbf{A}_{CV/CA}\mathbf{h}^{+}[k], \tag{6}$$

where

$$\mathbf{A}_{CV} = \begin{bmatrix} 1 & T & 0 \\ 0 & 1 & 0 \\ 0 & 0 & 0 \end{bmatrix}, \mathbf{A}_{CA} = \begin{bmatrix} 1 & T & 0.5T^2 \\ 0 & 1 & T \\ 0 & 0 & 1 \end{bmatrix}, \tag{7}$$

and T is the time interval of the MSS measurement. The state estimation covariance $\mathbf{P}$ follows the nominal propagation step:

$$\mathbf{P}^-[k+1] = \mathbf{A}_{CA/CV}\mathbf{P}^+[k]\mathbf{A}_{CA/CV}^{\mathrm{T}} + \mathbf{Q}, \tag{8}$$

where $\mathbf{Q}$ denotes the covariance matrix of the process noise in the system.

We denote the Kalman gain matrix as

$$\mathbf{K}[k+1] = \mathbf{P}^-[k+1]\mathbf{H}^{\mathrm{T}}\left(\mathbf{H}\mathbf{P}^-[k+1]\mathbf{H}^{\mathrm{T}} + \mathbf{R}\right)^{-1}, \tag{9}$$

where $\mathbf{R}$ is the measurement noise covariance. Following the standard Kalman update steps, we obtain the filtering values $\mathbf{h}^+[k+1]$ and $\mathbf{P}^+[k+1]$ as:

$$\mathbf{h}^+[k+1] = \mathbf{h}^-[k+1] + \mathbf{K}[k+1]\left(y[k+1] - \mathbf{H}\mathbf{h}^-[k+1]\right), \tag{10}$$

$$\mathbf{P}^+[k+1] = (\mathbf{I} - \mathbf{K}[k+1]\mathbf{H})\mathbf{P}^-[k+1]. \tag{11}$$

To facilitate concise expression, we introduce the Kalman filter procedure $\mathcal{F}_{CV/CA}$ as a representation of the two filtering models of CV or CA, implemented in different GNSS-R platforms. The function is defined as follows:

$$\left(\mathbf{h}^+[k+1], \mathbf{P}^+[k+1]\right) = \mathcal{F}_{CV/CA}\left(\mathbf{h}^+[k], \mathbf{P}^+[k]\right). \tag{12}$$

2.4. IMM-KF Method Designing and Implementing

IMM is a technique for estimating the target state by employing multiple models. These models' outcomes are fused using a proportional fusion strategy to achieve a more adaptable estimation model. Based on the Kalman filter, we designed the IMM-KF method to filter the retrieved result. The fundamental principles of the IMM-KF encompass input interaction, parallel filter state estimation, likelihood function updating, model probability adjustment, and output fusion. During this process, the initial information undergoes an input interaction step, followed by state estimation using parallel filters. Subsequently, the likelihood function is employed to update and adjust the model probability, while the Markov state transition matrix facilitates the model transmitting. Finally, the output is generated and integrated to produce the final estimation outcome. We use four different models to operationalize the IMM-KF, building on the development and analysis of a discrete model of a single system in the subsection above.

2.4.1. Model Interactions

This paper employs four distinct models, which utilize the Kalman filter to predict and assess the observation. These models are subsequently integrated into the IMM-KF method. The probability vector of the four models is

$$\begin{aligned} u[k] &= \{u_1[k], u_2[k], u_3[k], u_4[k]\} \\ &= \{u_{CY,CV}[k], u_{CY,CA}[k], u_{FY,CV}[k], u_{FY,CA}[k]\}. \end{aligned} \tag{13}$$

Here, CY is short for the CYGNSS platform, and FY is short for the FY-3E platform. At each time step k, the sum of the state distributions of the four models is 1, denoted as:

$$\sum_{j=1}^{4} u_j[k] = 1. \tag{14}$$

where j represents the jth model, whose range is 1 to 4 in this paper. In other words, $u_j[k]$ is the probability of the target being in model j at time k. The transition process between the models adheres to the principles of the Markov process. Therefore, we can define the state transition probability matrix as follows:

$$\boldsymbol{\mathcal{P}} = \begin{bmatrix} p_{11} & \cdots & p_{14} \\ \vdots & \ddots & \vdots \\ p_{41} & \cdots & p_{44} \end{bmatrix}. \tag{15}$$

The symbol $\boldsymbol{\mathcal{P}}$ denotes the probability p_{ij} associated with the transition from model i to model j. The sub-model's state estimation value from the previous time and its corresponding covariance are utilized to approximate the present time value. The initial value can be calculated using the Markov transition probability and the model probability matrix. Given that the model is currently at the $k - th$, the initial probability of the filter is established:

$$u_{ij}[k] = p_{ij}u_i[k]/c_j[k], \tag{16}$$

$$c_j[k] = \sum_{i=1}^{4} p_{ij}u_i[k], \tag{17}$$

where $u_{ij}[k]$ is the conditional probability associated with the transition from model i to model j at time k. $c_j[k]$ represents the probability of being in model j after the input interaction.

2.4.2. Filter Input Calculation

The model input variables and their corresponding covariances for each filter at the time k are computed. Based on the Kalman filter, the output can be obtained according to the following equations:

$$\hat{\mathbf{h}}_{0,j}[k] = \sum_{i=1}^{4} \mathbf{h}_i[k]u_{i,j}[k], \tag{18}$$

$$\mathbf{P}_{0,j}[k] = \sum_{i=1}^{4} u_{i,j}[k].\left\{\mathbf{P}_i[k] + \left[\widehat{\mathbf{h}}_i[k] - \widehat{\mathbf{h}}_j[k]\right]\left[\widehat{\mathbf{h}}_i[k] - \widehat{\mathbf{h}}_j[k]\right]^{\mathrm{T}}\right\}, \tag{19}$$

where $\hat{\mathbf{h}}_{0,j}[k]$ and $\mathbf{P}_{0,j}[k]$ represent the predicted state and the covariance matrix of the model j after the interaction.

2.4.3. Parallel Kalman Filtering

Within the IMM-KF, the input data are input to the selected filter model, which performs state estimation, filtering processing, and prediction. Maintaining the accuracy and performance of each corresponding Kalman filter model is imperative by ensuring that the input data are updated on time at each time step.

As mentioned before, $\mathcal{F}$ is used in this step. According to the provided data, it is possible to acquire four distinct filters, with their respective formulas being as follows:

$$\begin{aligned}
\left(\mathbf{h}_{CY,CV}[k+1], \mathbf{P}^{+}_{CY,CV}[k+1]\right) &= \mathcal{F}_{CV}(\mathbf{h}_{0,CY,CV}[k], \mathbf{P}_{0,CY,CV}[k]) \\
\left(\mathbf{h}_{CY,CA}[k+1], \mathbf{P}^{+}_{CY,CA}[k+1]\right) &= \mathcal{F}_{CA}(\mathbf{h}_{0,CY,CA}[k], \mathbf{P}_{0,CY,CA}[k]) \\
\left(\mathbf{h}_{FY,CV}[k+1], \mathbf{P}^{+}_{FY,CV}[k+1]\right) &= \mathcal{F}_{CV}(\mathbf{h}_{0,FY,CV}[k], \mathbf{P}_{0,FY,CV}[k]) \\
\left(\mathbf{h}_{FY,CA}[k+1], \mathbf{P}^{+}_{FY,CA}[k+1]\right) &= \mathcal{F}_{CA}(\mathbf{h}_{0,FY,CA}[k], \mathbf{P}_{0,FY,CA}[k])
\end{aligned} \tag{20}$$

2.4.4. The Maximum Likelihood Estimation Equation Construction

The statistical technique of maximum likelihood estimation is a commonly employed method for determining the values of unknown parameters based on observed data. The maximum likelihood equation is employed in the IMM-KF to determine the optimal filtering model that generates a state estimate that exhibits a high degree of similarity with the observed data. A joint probability function is derived by multiplying the prior probability of the system state with the likelihood function of the observed data. Maximizing the joint probability function determines the optimal model and its corresponding state estimate.

The optimal filtering model can be determined by maximizing a maximum likelihood equation utilizing the available observed data. Different models demonstrate various degrees of performance and adaptability. The attainment of precise and dependable state estimation outcomes can be facilitated by identifying the most suitable model. It can also include ambiguity in the observed data and system state, producing a more accurate estimate. The process can effectively measure uncertainty and appropriately allocate weights to various models based on uncertainty, yielding more rational outcomes. The maximum likelihood equation is employed in the IMM-KF to facilitate the dynamic switching of filtering models. Over time, as observational data evolve, the maximum likelihood equation can select a filtering model best suited for the current state. This process enhances the filter's performance and resilience. Various filtering models are employed to derive benefits. Diverse models may exhibit superior performance under varying circumstances. By employing the maximum likelihood equation for state fusion and weighting, it is possible to enhance state estimation's precision by amalgamating individual models' outcomes. Then, we can construct the maximum likelihood equation at time $k+1$:

$$L_j[k] = \frac{1}{\sqrt{(2\pi)^{\beta}\left|\mathbf{S}_j[k+1]\right|}} \cdot e^{-\frac{1}{2}\left(\tilde{y}_j[k+1]^T S_j[k+1]^{-1}\tilde{y}_j[k+1]\right)}, \tag{21}$$

where β is the dimension of the model. And $\tilde{y}_j[k+1]$ represents the innovation, and $\mathbf{S}_j[k+1]$ represents the covariance matrix, which can be expressed as:

$$\tilde{y}_j[k+1] = y[k+1] - \mathbf{H}_j[k+1]\hat{\mathbf{h}}_j[k+1], \tag{22}$$

$$\mathbf{S}_j[k+1] = \mathbf{H}_j[k+1]\mathbf{P}_j[k]\mathbf{H}_j[k+1]^T + \mathbf{R}[k+1]. \tag{23}$$

The state probability distribution of the updated model j can be represented as follows:

$$u_j[k+1] = \frac{L_j[k+1]u_j[k+1]}{\sum_{j=1}^{4} L_j[k+1]u_j[k+1]} \tag{24}$$

Thus, the state estimate $\mathbf{h}[k+1]$ and the corresponding covariance matrix $\mathbf{P}[k+1]$ can be obtained by

$$\hat{\mathbf{h}}[k+1] = \sum_{j=1}^{4} \hat{\mathbf{h}}_j[k]u_j[k+1], \tag{25}$$

$$\mathbf{P}[k+1] = \sum_{j=1}^{4}\left[\begin{array}{l} P_j[k+1]+ \\ \left(\hat{\mathbf{h}}_j[k+1]-\hat{\mathbf{h}}[k+1]\right)\left(\hat{\mathbf{h}}_j[k+1]-\hat{\mathbf{h}}[k+1]\right)^T \end{array}\right] \cdot u_j[k+1]. \tag{26}$$

The operational procedure of the IMM-KF for retrieving sea height, shown in Figure 5, iteratively processes sea surface altimetry measurements.

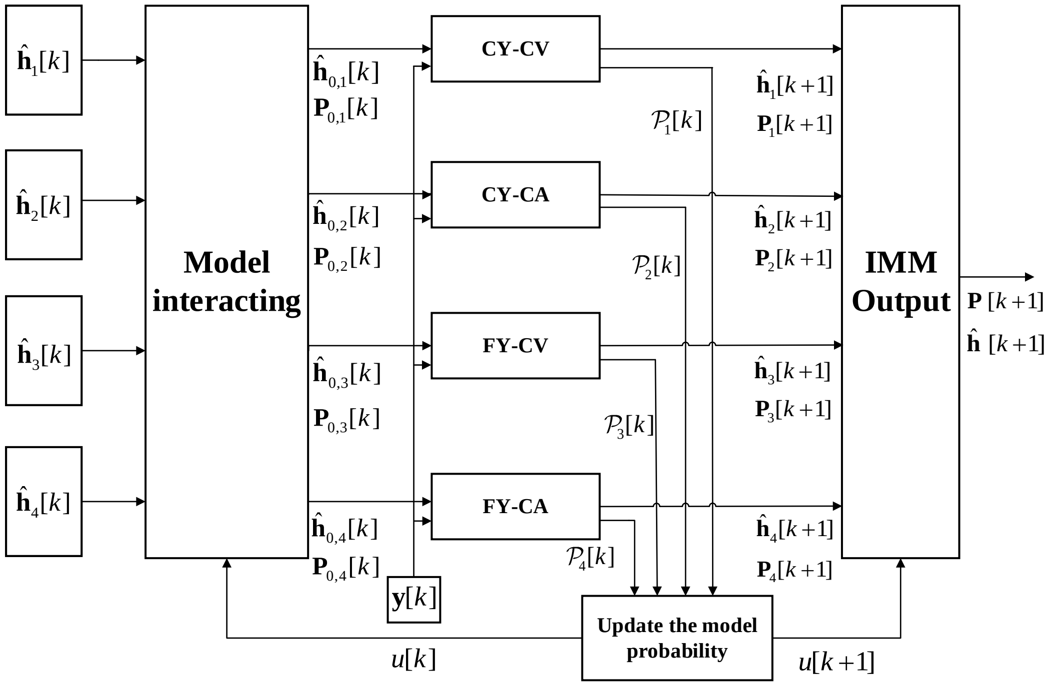

Figure 5. Model working schematic.

3. Results and Analysis

3.1. Machine Learning Retrieved Results

Data from the CYGNSS and FY-3E platforms during 1–17 August 2022 are used. The data from the first and second days of August are used for training. The input data for predicting SSH are derived from the feature information extracted from each reflection event. The label is produced based on the DTU model, which is explained in Section II. As shown in Figure 6, although FY-3E provides fewer data than CYGNSS, it can also pick up signals from the Galileo and Beidou systems in addition to GPS. Additionally, its range of latitude is wider than CYGNSS's. The color bar shows the retrieved SSH in the map.

During the data processing phase, the initial step involves implementing data quality control. This process includes filtering the two spaceborne GNSS-R product datasets based on their respective flags, excluding data with low SNR and specular points on land. Furthermore, we choose the DDMs where the peak bin is not in the first/last row/column.

Due to CYGNSS's latitude limitations (-40 to 40 degrees), it is appropriate to apply the IMM-KF approach. The neural network is trained in a GPU environment using the NVIDIA GeForce RTX 4090, with an average duration of approximately two hours.

After obtaining SSH values for each specular point, we divide the points into a dataset every 8 h. Following this, the worldwide map is divided into a cell with dimensions of 0.25 ° by 0.25 °, and the average measurement of multiple specular scattering points in each cell is calculated. Next, a two-dimensional interpolation is performed on the worldwide gridded map, leading to the computation of the MSS map for the specified 8-hour time period. However, the limited number of FY-3E points is identified as the reason for the impracticality of performing two-dimensional interpolation. Therefore, a sliding window mean is utilized, with a window size of three temporal intervals and a shift of one temporal interval. This ensures the availability of sufficient specular reflection points to facilitate two-dimensional interpolation during each temporal interval. This study produces 51 global MSS maps by utilizing the data over 17 days. The output consists of an 8-hourly depiction of the global MSS map for CYGNSS and FY-3E. This research utilizes a temporal resolution of 8 h and a spatial resolution of $0.25° \times 0.25°$.

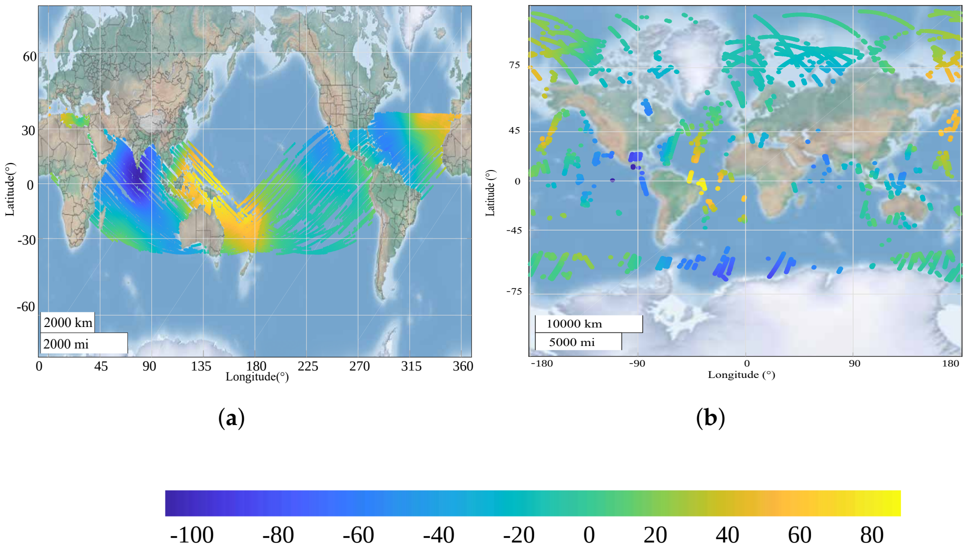

Figure 6. Example tracks of CYGNSS and FY-3E. (**a**) CYGNSS track, (**b**) FY-3E track. (8 h for CYGNSS and 48 h for FY-3E.)

The convergence curves of the training are shown in Figure 7. The overall process demonstrates convergence, as shown by the curves plotted at the completion of the training process, corresponding to 36 and 60 iterations, respectively. These curves indicate that MAE tends to stabilize during the learning process.

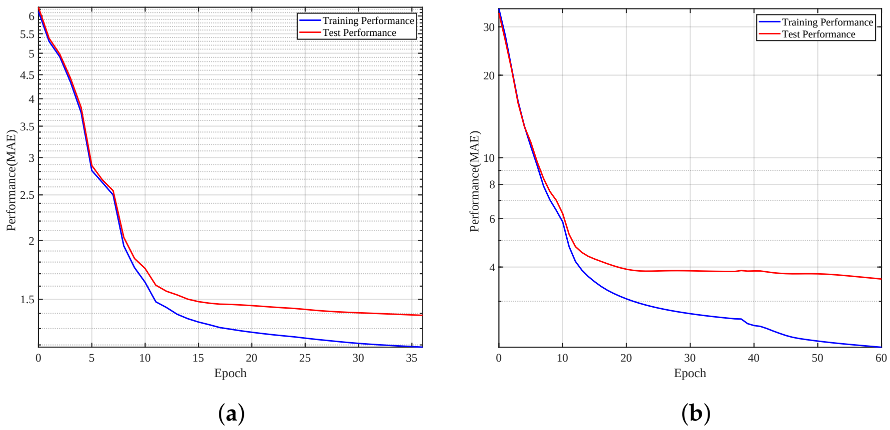

Figure 7. Convergence curve during network training. (**a**) CYGNSS, (**b**) FY-3E.

The data training prediction results are presented in Table 2 and Figure 8, indicating that both platforms demonstrate a high correlation coefficient with the true SSH, exceeding 99%. The correlation coefficient between the retrieved SSH data obtained by the CYGNSS platform and that of the FY-3E platform is marginally greater. This suggests that the ANN employed for predicting SSH for both spaceborne GNSS-R platforms has demonstrated initial efficacy with a degree of accuracy at the meter level. The RMSE values for the SSHs obtained through CYGNSS and FY-3E are 1.24 and 1.73 m, respectively. The results show that CYGNSS performs slightly better than FY-3E.

Furthermore, the Mean Absolute Error (MAE) values for the two platforms reached 0.85 and 1.28 m, respectively. The CYGNSS platform exhibits superior performance, resulting in a substantial data volume. Conversely, the FY-3E system has a restricted number of receiving equipment, and its latitude range spans from −90 to 90 degrees, thereby generating relatively fewer data during a given time. An additional factor contributing to the variation in outcomes is the utilization of a conventional and straightforward ANN in this study, without incorporating more intricate network architecture. The SSH at the meter level is retrieved using the ANN, providing a foundation for future IMM-KF methods.

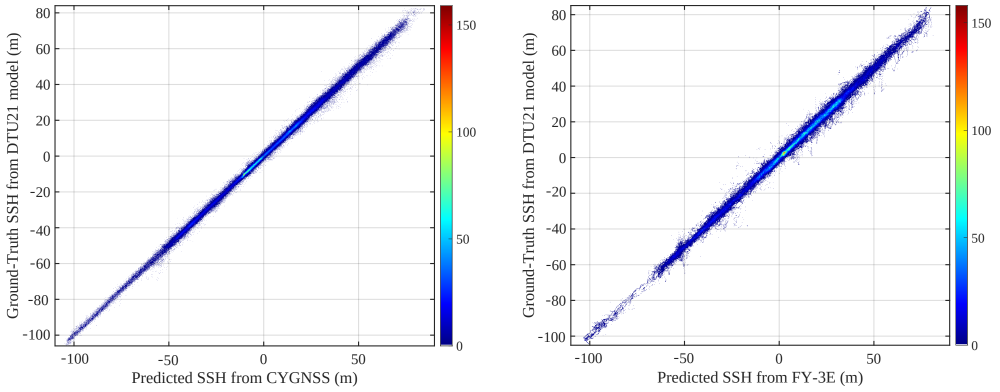

(**a**) (**b**)

Figure 8. The density map of CYGNSS—ground truth and FY-3E—ground truth. (**a**) Prediction from CYGNSS, (**b**) prediction from FY-3E.

Table 2. The SSH prediction results from CYGNSS and FY-3E.

	CYGNSS	**FY-3E**
MAE (m)	0.85	1.28
RMSE (m)	1.24	1.73
R^2 (%)	99.92	99.81

To further investigate the sensitivity of the neural network model under different conditions, we plotted the CYGNSS and FY-3E data based on the SNR, as illustrated in Figure 9. Subsequently, we conducted a segmented analysis. The results indicate that both of the spaceborne models' data show a good performance under high-SNR conditions. However, the scatter plot of FY-3E data reveals a less concentrated distribution of absolute errors compared to results retrieved from CYGNSS data. Table 3 demonstrates that performance metrics are superior under high-SNR conditions. This can be attributed to the fact that in high-SNR scenarios, which correspond to low wind speeds and favorable environments, the signal energy is more concentrated and the reflected signal data are less affected by environmental factors, leading to more accurate results. The findings suggest that both CYGNSS and FY-3E data exhibit consistency with respect to SNR, indicating that high-SNR conditions are more suitable for the neural network-based retrieval of the sea surface height.

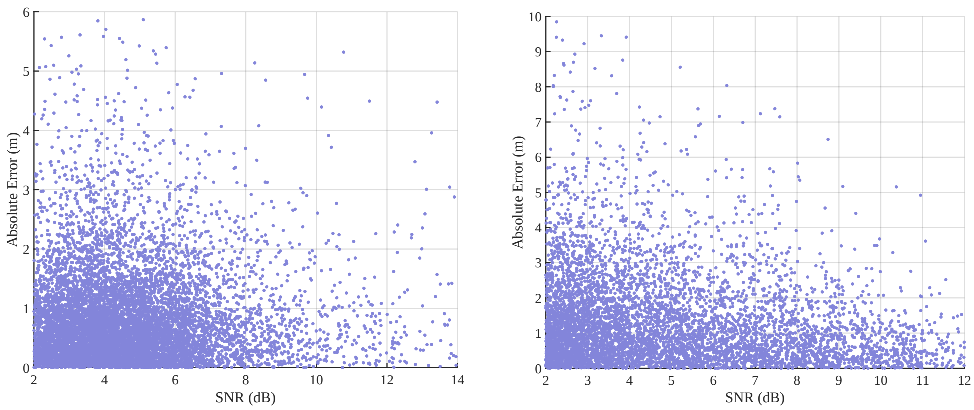

(**a**) (**b**)

Figure 9. The absolute error distribution of the different spaceborne SNR data. (**a**) CYGNSS, (**b**) FY-3E.

Table 3. The results in different SNR ranges.

	SNR (dB)	CYGNSS	FY-3E
MAE (m)	2–6	1.01	1.85
	6–10	0.90	1.74
	>10	0.82	1.61
RMSE (m)	2–6	1.30	1.85
	6–10	1.21	1.77
	>10	1.17	1.67
R^2 (%)	2–6	99.90	99.77
	6–10	99.93	99.82
	>10	99.95	99.84

3.2. IMM-KF Results and Analysis

We conduct IMM-KF processing on each cell in the time domain using 51 global MSS maps. A display grid cell has a latitude range of -6.75 to -6.5 degrees and a longitude range of 12.5 to 12.75 degrees. As illustrated in the previous subsection, CYGNSS and FY-3E have two models (CV and CA) to describe the MSS changing in the 8 h period.

The global MSS maps, obtained from observations of CYGNSS, FY-3E, and the DTU model during the first 8-hour time frame of August 1, are depicted in Figure 10. This figure illustrates significant similarity in the outcomes obtained from three distinct models. However, it is evident that there are significant differences in the MSS map in certain regions, such as at the location of 140° in longitude and 20° in latitude. The results obtained by retrieving CYGNSS and DTU models are similar, while FY-3E does not capture the SSH features of this particular region. The reason for incomplete global coverage during the specified period can be attributed to the inadequacy of specular reflection points in FY-3E. Consequently, in certain regions covered by only a subset of a few dispersed points, two-dimensional interpolation is necessary to acquire the MSS within each cell, leading to retrieval inaccuracies. Despite the sliding window averaging applied to the FY-3E data to mitigate noise in the global MSS, some global grids still exhibit MSS retrieval errors.

In the selected cell (a latitude range of -6.75 to -6.5 degrees and a longitude range of 12.5 to 12.75 degrees), as mentioned before, we collect the retrieved SSH from CYGNSS and FY-3E platforms. It is a fact that the reflection does not always occur in this cell. In this case, we use the average of the SSH to obtain the MSS for 8 h. The reflections from the CYGNSS and FY-3E platforms in 8 h are averaged, respectively.

As shown in Figure 11, the MSS values of 51 global maps within the selected cell are presented (the data are from 17 days, and three global maps can be obtained in a day). The utilization of the proposed IMM-KF technique based on two GNSS-R platforms is demonstrated by the MSS trend in the red line, while the yellow line represents the MSS trend of the DTU model. The figure illustrates notable deviations between the outcomes of FY-3E and the observed values on 4 August and 12 August. During this period, IMM-KF tends to rely on the CYGNSS model. From 13–17 August 2022, IMM-KF tends to place reliance on the outcomes derived from FY-3E. The IMM-KF approach can perform filtering and fusion on a continuously changing observation quantity, even with significant sampling point errors, by allocating distinct model probabilities.

Figure 12 displays the probability distribution of each time step's model for the four models designed in this article. The figure illustrates that the model probability of CYGNSS is comparatively higher during the observed period, owing to the high precision of CYGNSS data. From August 4 to August 6, the CY-CA model probability is found to be the predominant component among the four model probability distributions. This observation suggests that the model's acceleration is consistent throughout and is primarily influenced by the results established through CYGNSS retrieval. During the period from

12–14 August 2022, there is a tendency for the MSS to exhibit a more uniform pattern of change.

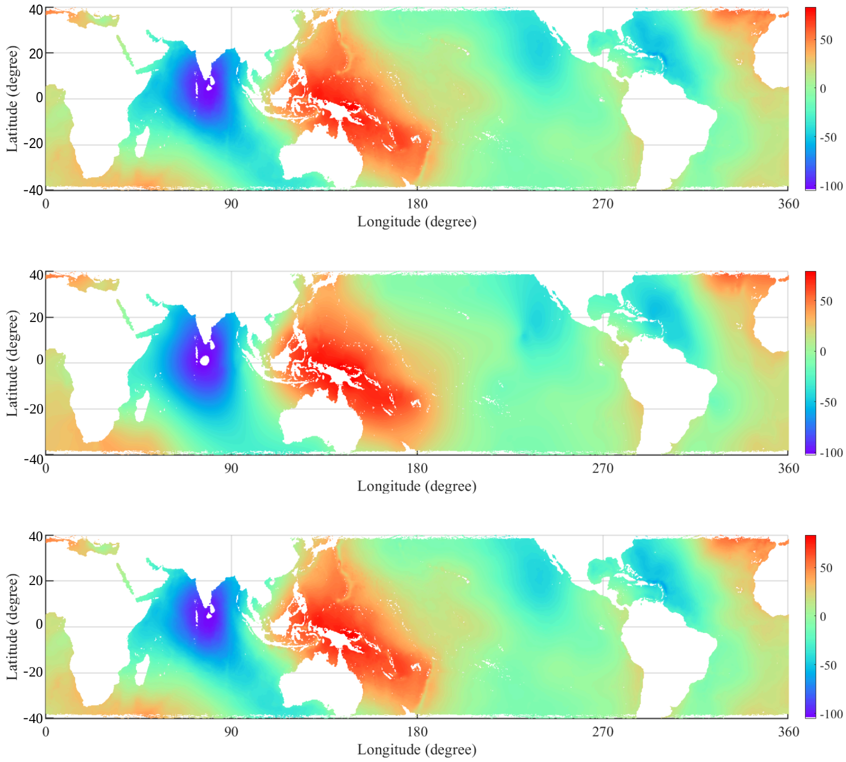

Figure 10. MSS maps on August 1st. The data sources from top to bottom are CYGNSS, FY-3E, DTU21.

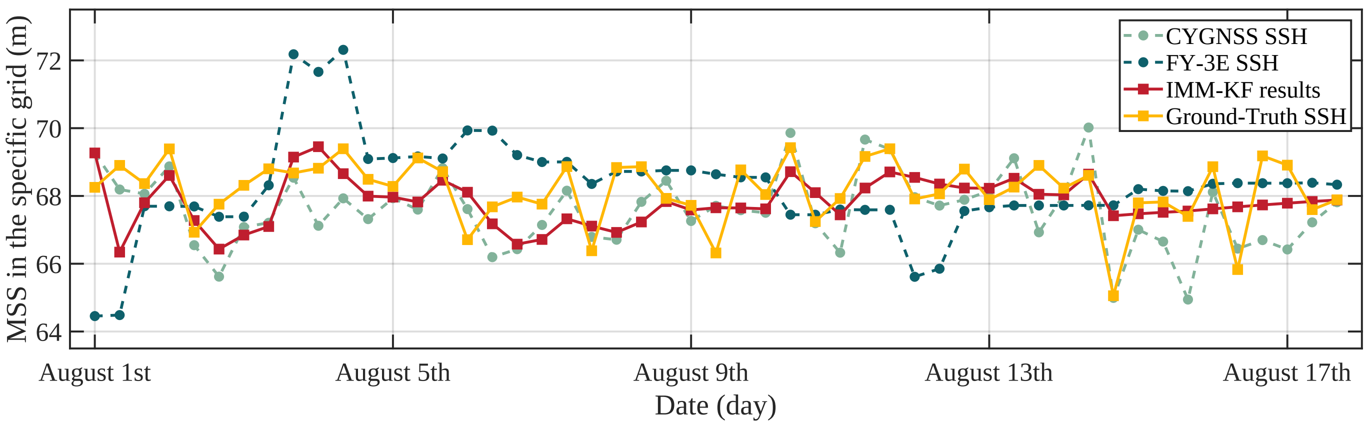

Figure 11. The MSS result based on IMM-KF during the 17 days.

Additionally, it is observed that the probability of the CY-CV model reaches its maximum value, approaching unity. Compared to the CYGNSS model, the probability of the FY-3E model is comparatively lower, particularly in the case of the FY-CA model, which makes a relatively more minor contribution to the overall IMM-KF. The explanation for this could be attributed to the reduced data precision of FY-3E, which poses challenges in providing a precise depiction of the CA model. After 14 August, the likelihood of the FY-3E model exhibits a consistent increase compared to the CYGNSS model. Moreover, the probability of the FY-CV model approaches unity during this interval, signifying its efficacy in accurately characterizing and forecasting MSS. The model employs an adaptive approach and selects a model that relies on FY-3E data, which exhibit comparatively smoother and more stable characteristics than those of CYGNSS. This observation also indicates the accuracy and efficacy of the model. The statistical results indicate that the RMSE of CYGNSS's MSS is 1.15 m, while the RMSE of FY-3E's MSS is 1.65 m. Additionally, the IMM-KF approach reaches an RMSE of 1.03 m, which provides evidence for the efficacy of the method proposed in this paper.

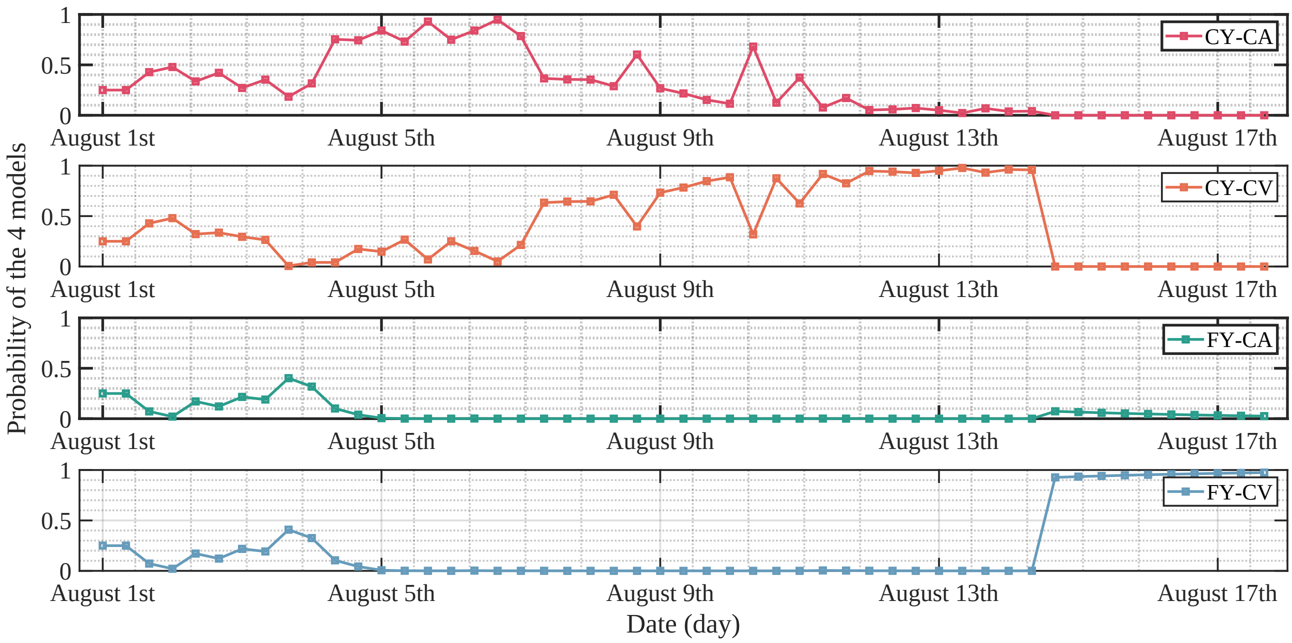

Figure 12. The probability of each model during the time.

4. Conclusions

This paper focuses on the interaction of the models using CYGNSS and FY-3E GNSS measurements. First, this study constructs an artificial neural network to retrieve SSH, which includes different layers and nodes. The study involves training and making predictions using a dataset from 1–17 August 2022. The analytical findings demonstrate that the correlation coefficients between the retrieved SSH from both platforms and DTU21 >99%. The RMSE values for CYGNSS and FY-3E are 1.24 and 1.73 m, respectively. These results indicate that CYGNSS data show higher accuracy due to the larger dataset compared to the FY-3E platform.

Following that, we introduce the IMM-KF approach. The introduction of the IMM-KF method highlights the importance of interaction between multiple models and improves the accuracy and robustness of estimation by dynamically switching between different dynamic models, so as to effectively deal with SSH estimation in complex environments. The study employs an 8 h time interval and discretizes the global region into spatial domain cells with dimensions of $0.25° \times 0.25°$ of latitude and longitude. The IMM-KF methodology is implemented by creating four distinct models: CY-CV, CY-CA, FY-CV, and FY-CA. Each model performs Kalman filtering for its specific state and then combines the models at each time step, while adjusting the model probabilities accordingly to generate the most favorable outcome. It is obvious that this approach dynamically adjusts the probabilities assigned to each model at varying time intervals. This adaptive mechanism facilitates the integration of multiple systems and models through the process of amalgamation filtering. The results reveal that the RMSE values for CYGNSS and FY-3E in the selected location cell are 1.15 and 1.65 m, respectively. Nevertheless, the IMM-KF approach presents the ability to improve these results to an RMSE of 1.03 m.

Our future research will focus on improving and expanding our models to more effectively encompass a broader spectrum of dynamic fluctuations in SSH. This expansion is expected to lead to a deeper and more complex understanding of these differences. Furthermore, we are presently engaged in comprehensive research to identify supplementary data sources with the aim of enhancing the accuracy and precision of ocean altimetry observations. These strategic advances are anticipated to significantly enhance the field of sea surface height measurement, signifying a substantial advancement in this specialized area.

Author Contributions: Conceptualization, J.X., D.Y. and Z.Z.; methodology, J.X. and F.W.; software, J.X.; validation, J.X., Z.Z. and F.W.; formal analysis, J.X.; investigation, J.X. and Z.Z.; resources, D.Y.; data curation, Z.Z. and F.W.; writing—original draft preparation, J.X.; writing—review and editing, F.W. and D.Y.; visualization, J.X. and Z.Z.; supervision, F.W. and D.Y.; project administration, D.Y. All authors have read and agreed to the published version of the manuscript.

Funding: This research received no external funding.

Data Availability Statement: CYGNSS data is available at https://cmr.earthdata.nasa.gov/virtual-directory/collections/C2146321631-POCLOUD (accessed on 18 April 2024). FY-3E data is available at http://satellite.nsmc.org.cn/portalsite/default.aspx (accessed on 18 April 2024).

Conflicts of Interest: The authors declare no conflicts of interest.

References

1. Cazenave, A.; Cozannet, G.L. Sea level rise and its coastal impacts. *Earth Future* **2014**, *2*, 15–34. [CrossRef]
2. Hauer, M.E.; Fussell, E.; Mueller, V.; Burkett, M.; Call, M.; Abel, K.; McLeman, R.; Wrathall, D. Sea-level rise and human migration. *Nat. Rev. Earth Environ.* **2020**, *1*, 28–39. [CrossRef]
3. Mu, D.; Xu, T.; Guan, M. Sea level instantaneous budget for 2003–2015. *Geophys. J. Int.* **2022**, *229*, 828–837. [CrossRef]
4. Abdalla, S.; Kolahchi, A.A.; Ablain, M.; Adusumilli, S.; Bhowmick, S.A.; Alou-Font, E.; Amarouche, L.; Andersen, O.B.; Antich, H.; Aouf, L.; et al. Altimetry for the future: Building on 25 years of progress. *Adv. Space Res.* **2021**, *68*, 319–363. [CrossRef]
5. Benveniste, J.; Cazenave, A.; Vignudelli, S.; Fenoglio-Marc, L.; Shah, R.; Almar, R.; Andersen, O.; Birol, F.; Bonnefond, P.; Bouffard, J.; et al. Requirements for a coastal hazards observing system. *Front. Mar. Sci.* **2019**, *6*, 348. [CrossRef]
6. Ehsan, S.; Begum, R.A.; Nor, N.G.M.; Maulud, K.N.A. Current and potential impacts of sea level rise in the coastal areas of Malaysia. *IOP Conf. Ser. Earth Environ. Sci.* **2019**, *228*, 012023. [CrossRef]
7. Martinez-Felix, C.A.; Vazquez-Becerra, G.E.; Geremia-Nievinski, F.; Millan-Almaraz, J.R.; Franco-Ochoa, C.; Melgarejo-Morales, A.; Gaxiola-Camacho, J.R. Tidal measurements in the Gulf of Mexico: Intercomparison of coastal tide gauge, insular GNSS reflectometry and SAR altimetry. *GPS Solut.* **2022**, *26*, 22. [CrossRef]
8. Ballarotta, M.; Ubelmann, C.; Pujol, M.I.; Taburet, G.; Fournier, F.; Legeais, J.F.; Faugère, Y.; Delepoulle, A.; Chelton, D.; Dibarboure, G.; et al. On the resolutions of ocean altimetry maps. *Ocean Sci.* **2019**, *15*, 1091–1109. [CrossRef]
9. Li, W.; Cardellach, E.; Fabra, F.; Ribó, S.; Rius, A. Assessment of spaceborne GNSS-R ocean altimetry performance using CYGNSS mission raw data. *IEEE Trans. Geosci. Remote Sens.* **2019**, *58*, 238–250. [CrossRef]
10. Tye, J.; Jales, P.; Unwin, M.; Underwood, C. The first application of stare processing to retrieve mean square slope using the SGR-ReSI GNSS-R experiment on TDS-1. *IEEE J. Sel. Top. Appl. Earth Obs. Remote Sens.* **2016**, *9*, 4669–4677. [CrossRef]
11. Carreno-Luengo, H.; Crespo, J.A.; Akbar, R.; Bringer, A.; Warnock, A.; Morris, M.; Ruf, C. The CYGNSS mission: On-going science team investigations. *Remote Sens.* **2021**, *13*, 1814. [CrossRef]
12. Niu, X.; Lu, F.; Liu, Y.; Jing, C.; Wan, B. Application and technology of Bufeng-1 GNSS-R demonstration satellites on sea surface wind speed detection. *Lect. Notes Electr. Eng.* **2020**, *650*, 206–213.
13. Nan, Y.; Ye, S.; Liu, J.; Guo, B.; Zhang, S.; Li, W. Signal-to-noise ratio analyses of spaceborne GNSS-reflectometry from Galileo and BeiDou satellites. *Remote Sens.* **2021**, *14*, 35. [CrossRef]
14. Zhang, T.; Yang, L.; Nan, H.; Yin, C.; Sun, B.; Yang, D.; Hong, X.; Lopez-Baeza, E. In-Situ GNSS-R and Radiometer Fusion Soil Moisture Retrieval Model Based on LSTM. *Remote Sens.* **2023**, *15*, 2693. [CrossRef]
15. Rodriguez-Alvarez, N.; Monerris, A.; Bosch-Lluis, X.; Camps, A.; Vall-Llossera, M.; Marchan-Hernández, J.F.; Ramos-Perez, I.; Valencia, E.; Martínez-Fernández, J.; Sánchez-Martín, N.; et al. Soil moisture and vegetation height retrieval using GNSS-R techniques. In Proceedings of the 2009 IEEE International Geoscience and Remote Sensing Symposium, Cape Town, South Africa, 12–17 July 2009; Volume 3, pp. III-869–III-872. [CrossRef]
16. Yan, Q.; Huang, W.; Jin, S.; Jia, Y. Pan-tropical soil moisture mapping based on a three-layer model from CYGNSS GNSS-R data. *Remote Sens. Environ.* **2020**, *247*, 111944. [CrossRef]
17. Hu, Y.; Jiang, Z.; Liu, W.; Yuan, X.; Hu, Q.; Wickert, J. GNSS-R Sea Ice Detection Based on Linear Discriminant Analysis. *IEEE Trans. Geosci. Remote Sens.* **2023**. [CrossRef]
18. Yan, Q.; Huang, W. Sea ice remote sensing using GNSS-R: A review. *Remote Sens.* **2019**, *11*, 2565. [CrossRef]
19. Li, W.; Cardellach, E.; Fabra, F.; Ribó, S.; Rius, A. Measuring Greenland ice sheet melt using spaceborne GNSS reflectometry from TechDemoSat-1. *Geophys. Res. Lett.* **2020**, *47*, e2019GL086477. [CrossRef]
20. Xie, Y.; Yan, Q. Stand-Alone Retrieval of Sea Ice Thickness From FY-3E GNOS-R Data. *IEEE Geosci. Remote Sens. Lett.* **2024**, *21*, 2000305. [CrossRef]

21. Downs, B.; Kettner, A.J.; Chapman, B.D.; Brakenridge, G.R.; O'Brien, A.J.; Zuffada, C. Assessing the Relative Performance of GNSS-R Flood Extent Observations: Case Study in South Sudan. *IEEE Trans. Geosci. Remote Sens.* **2023**, *61*, 1–13. [CrossRef]
22. Yan, Q.; Liu, S.; Chen, T.; Jin, S.; Xie, T.; Huang, W. Mapping Surface Water Fraction Over the Pan-Tropical Region Using CYGNSS Data. *IEEE Trans. Geosci. Remote Sens.* **2024**, *62*, 1–14. [CrossRef]
23. Bu, J.; Yu, K.; Zuo, X.; Ni, J.; Li, Y.; Huang, W. GloWS-Net: A Deep Learning Framework for Retrieving Global Sea Surface Wind Speed Using Spaceborne GNSS-R Data. *Remote Sens.* **2023**, *15*, 590. [CrossRef]
24. Rodriguez-Alvarez, N.; Munoz-Martin, J.F.; Morris, M. Latest Advances in the Global Navigation Satellite System—Reflectometry (GNSS-R) Field. *Remote Sens.* **2023**, *15*, 2157. [CrossRef]
25. Zhang, Y.; Zheng, W.; Liu, Z. Improving the spaceborne GNSS-R altimetric precision based on the novel multilayer feedforward neural network weighted joint prediction model. *Def. Technol.* **2024**, *32*, 271–284. [CrossRef]
26. Cheng, Z.; Jin, T.; Chang, X.; Li, Y.; Wan, X. Evaluation of spaceborne GNSS-R based sea surface altimetry using multiple constellation signals. *Front. Earth Sci.* **2023**, *10*, 1079255. [CrossRef]
27. Martin-Neira, M. A passive reflectometry and interferometry system (PARIS): Application to ocean altimetry. *ESA J.* **1993**, *17*, 331–355.
28. Saynisch, J.; Semmling, M.; Wickert, J.; Thomas, M. Potential of space-borne GNSS reflectometry to constrain simulations of the ocean circulation: A case study for the South African current system. *Ocean Dyn.* **2015**, *65*, 1441–1460. [CrossRef]
29. Clarizia, M.P.; Ruf, C.; Cipollini, P.; Zuffada, C. First spaceborne observation of sea surface height using GPS-Reflectometry. *Geophys. Res. Lett.* **2016**, *43*, 767–774. [CrossRef]
30. Li, W.; Cardellach, E.; Fabra, F.; Rius, A.; Ribó, S.; Martín-Neira, M. First spaceborne phase altimetry over sea ice using TechDemoSat-1 GNSS-R signals. *Geophys. Res. Lett.* **2017**, *44*, 8369–8376. [CrossRef]
31. Mashburn, J.; Axelrad, P.; Lowe, S.T.; Larson, K.M. Global ocean altimetry with GNSS reflections from TechDemoSat-1. *IEEE Trans. Geosci. Remote Sens.* **2018**, *56*, 4088–4097. [CrossRef]
32. Cardellach, E.; Li, W.; Rius, A.; Semmling, M.; Wickert, J.; Zus, F.; Ruf, C.S.; Buontempo, C. First Precise Spaceborne Sea Surface Altimetry With GNSS Reflected Signals. *IEEE J. Sel. Top. Appl. Earth Obs. Remote Sens.* **2020**, *13*, 102–112. [CrossRef]
33. Wang, Y.; Morton, Y.J. Coherent reflections using closed-loop PLL processing of CYGNSS IF data. In Proceedings of the IGARSS 2019—2019 IEEE International Geoscience and Remote Sensing Symposium, Yokohama, Japan 28 July–2 August 2019; IEEE: New York, NY, USA, 2019; pp. 8737–8740.
34. Wang, Y.; Morton, Y. Coherent and semi-coherent spaceborne GNSS-R for land surface altimetry applications. In Proceedings of the 33rd International Technical Meeting of the Satellite Division of The Institute of Navigation (ION GNSS+ 2020), Virtual, 21–25 September 2020; pp. 3901–3908.
35. Mashburn, J.; Axelrad, P.; Zuffada, C.; Loria, E.; O'Brien, A.; Haines, B. Improved GNSS-R ocean surface altimetry with CYGNSS in the seas of Indonesia. *IEEE Trans. Geosci. Remote Sens.* **2020**, *58*, 6071–6087. [CrossRef]
36. Hu, C.; Benson, C.R.; Qiao, L.; Rizos, C. The validation of the weight function in the leading-edge-derivative path delay estimator for space-based GNSS-R altimetry. *IEEE Trans. Geosci. Remote Sens.* **2020**, *58*, 6243–6254. [CrossRef]
37. Zhang, G.; Xu, Z.; Wang, F.; Yang, D.; Xing, J. Evaluation and correction of elevation angle influence for coastal GNSS-R ocean altimetry. *Remote Sens.* **2021**, *13*, 2978. [CrossRef]
38. Zhang, Y.; Huang, S.; Han, Y.; Yang, S.; Hong, Z.; Ma, D.; Meng, W. Machine learning methods for spaceborne GNSS-R sea surface height measurement from TDS-1. *IEEE J. Sel. Top. Appl. Earth Obs. Remote Sens.* **2021**, *15*, 1079–1088. [CrossRef]
39. Arabi, S.; Asgarimehr, M.; Kada, M.; Wickert, J. Hybrid CNN-LSTM Deep Learning for Track-Wise GNSS-R Ocean Wind Speed Retrieval. *Remote Sens.* **2023**, *15*, 4169. [CrossRef]
40. Xing, J.; Yang, D.; Zhang, Z.; Yang, P.; Wang, F. Development of F-ResNet for Spaceborne GNSS-R Sea Surface Height Measurement From CYGNSS. *IEEE Commun. Lett.* **2023**, *27*, 2712–2716. [CrossRef]
41. Ansari, K.; Seok, H.W.; Jamjareegulgarn, P. Quasi zenith satellite system-reflectometry for sea-level measurement and implication of machine learning methodology. *Sci. Rep.* **2022**, *12*, 21445. [CrossRef] [PubMed]
42. Li, W.; Cardellach, E.; Ribó, S.; Oliveras, S.; Rius, A. Exploration of multi-mission spaceborne GNSS-R raw IF data sets: Processing, data products and potential applications. *Remote Sens.* **2022**, *14*, 1344. [CrossRef]
43. Kong, X.; Zhang, X.; Zhang, X.; Wang, C.; Chiang, H.D.; Li, P. Adaptive dynamic state estimation of distribution network based on interacting multiple model. *IEEE Trans. Sustain. Energy* **2021**, *13*, 643–652. [CrossRef]
44. Lim, J.; Kim, H.S.; Park, H.M. Interactive-multiple-model algorithm based on minimax particle filtering. *IEEE Signal Process. Lett.* **2019**, *27*, 36–40. [CrossRef]
45. Fan, X.; Wang, G.; Han, J.; Wang, Y. Interacting multiple model based on maximum correntropy Kalman filter. *IEEE Trans. Circuits Syst. II Express Briefs* **2021**, *68*, 3017–3021. [CrossRef]
46. Zavorotny, V.U.; Voronovich, A.G. Scattering of GPS signals from the ocean with wind remote sensing application. *IEEE Trans. Geosci. Remote Sens.* **2000**, *38*, 951–964. [CrossRef]
47. Zhang, P.; Hu, X.; Lu, Q.; Zhu, A.; Lin, M.; Sun, L.; Chen, L.; Xu, N. *FY-3E: The First Operational Meteorological Satellite Mission in an Early Morning Orbit*; Springer: Berlin/Heidelberg, Germany, 2022.

48. Wang, Q.; Zheng, W.; Wu, F.; Zhu, H.; Xu, A.; Shen, Y.; Zhao, Y. Information Fusion for Spaceborne GNSS-R Sea Surface Height Retrieval Using Modified Residual Multimodal Deep Learning Method. *Remote Sens.* **2023**, *15*, 1481. [CrossRef]
49. Andersen, O.B.; Rose, S.K.; Abulaitijiang, A.; Zhang, S.; Fleury, S. The DTU21 global mean sea surface and first evaluation. *Earth Syst. Sci. Data Discuss.* **2023**, *2023*, 1–19. [CrossRef]